Title

Understanding differences in quantification of conventional versus experimental contrast materials with different clinical dual-energy computed tomography systems, and development of universal contrast quantification “handshake”

Author

Shu, Samuel Philip

Publication Date

2019

Peer reviewed|Thesis/dissertation

Understanding differences in quantification of conventional versus experimental contrast materials with different clinical dual-energy computed tomography systems, and development of universal contrast quantification “handshake”

by

Samuel Shu

THESIS

Submitted in partial satisfaction of the requirements for degree of

MASTER OF SCIENCE

in

Biomedical Imaging

in the

GRADUATE DIVISION

of the

UNIVERSITY OF CALIFORNIA, SAN FRANCISCO

Approved:

DocuSigned by:
Benjamin M Yeh
074C888E040E4E4...

Benjamin M Yeh

Chair

DocuSigned by:
Galateia Kazakia

Galateia Kazakia

DocuSigned by:
Susan Noworolski

Susan Noworolski

DocuSigned by:
Youngho Seo
C525AA918D85484...

Youngho Seo

Committee Members

Understanding differences in quantification of conventional versus experimental contrast materials with different clinical dual-energy computed tomography systems, and development of universal contrast quantification “handshake”

Samuel Shu

Abstract

Dual energy computed tomography (DECT) has unique imaging capabilities with the potential to improve clinical diagnosis compared to conventional single energy CT. The impending development of novel contrast agents that can take advantage of the unique material differentiation capability of DECT could dramatically expand the diagnostic value of this technology. Unfortunately, clinical DECT systems show intersystem variations in contrast quantification. These inter-scanner differences have been recognized to a limited extent in the current literature. A polyurethane abdominal phantom containing various conventional and experimental contrast materials was constructed to quantify the variance in Hounsfield units (HU) across six clinically available DECT systems. The attenuation profiles of conventional and novel contrast materials presented in this study may serve as a means to correct for intersystem differences across the DECT systems examined.

Table of Contents

List of Figures

List of Tables

Introduction: Dual energy computed tomography (DECT) has unique imaging capabilities with the potential to improve clinical diagnosis compared to conventional single energy CT. These include basis material decomposition to create virtual non-contrast and virtual monoenergetic image reconstructions with reduced beam hardening artifact and increased contrast-to-noise ratio.[1,2,3] The advantages of DECT have been hinted at over the past forty years, and most recently have become increasingly widespread in the past decade as every major CT manufacturer has now introduced scanners capable of rapid dual energy CT data acquisition.[4-9]

Clinical DECT, whereby two CT datasets are simultaneously or near-simultaneously acquired with different x-ray energy spectra, has been achieved by a number of hardware implementations including dual source, rapid kVp switching with a single source and dual-layered detector, sequential acquisition, and quantum-counting detector designs – the former two of which are clinically most common.[8] Each DECT hardware approach presents unique technical challenges to overcome in order to produce high-quality, clinically useful images. Dual source systems typically employ correction algorithms to address cross-scattering.[10] Single source systems must similarly account for overlap between high and low energy spectra.[11] One strategy to maximize spectral separation is the use of a tin filter to selectively attenuate low-energy photons from the intended high-energy spectrum.[9]

Basis material decomposition can be performed on a voxel-by-voxel basis to generate single-material images based on material-specific attenuation characteristics. Compton scattering and the photoelectric effect are the major phenomena that account for x-ray attenuation and are dependent on photon energy and atomic number of the

attenuating material. Therefore, materials differentiable by DECT must be of sufficiently disparate effective atomic number, with iodine and water (soft tissue) commonly assumed as basis materials.[8,12] From such basis material decomposition images, virtual monochromatic images (VMI) can be generated as a linear combination of the mass attenuation coefficients of the basis materials, with attenuation coefficients based on calibration measurements.[1,8,9,11,13] The specific postprocessing methods used to generate VMI as well as virtual non-contrast (VNC) images vary between manufacturers and are proprietary.[14] These operations can be performed in either the projection domain or image domain, with the former employed in the setting of DECT acquisition by single source fast kVp switching method and dual layer detector implementations.[1]

DECT holds great promise for improving clinical diagnosis, particularly regarding contrast material detection, differentiation, and quantification.[7] An exciting potential benefit of DECT is that multiple different contrast agents with different atomic composition may be delivered simultaneously and their signals digitally separated to provide multiple high-resolution, perfectly co-registered images with a single pass of the DECT scanner. The impending development of novel contrast agents that can take advantage of the unique material differentiation capability of DECT could dramatically expand the diagnostic value of this technology.[15] Unfortunately, clinical DECT systems show intersystem variations in contrast quantification. These inter-scanner differences have been recognized to a limited extent in the current literature.[13,16] My study aims to quantify the variance in Hounsfield units (HU) across six clinically available DECT systems and develop a universal contrast quantification by proposing a means to correct for intersystem differences. Currently, DECT data can only be processed using

vendor-specific software, presenting challenges to clinical workflow. My study will also address the possibility of generating virtual monoenergetic images using a vendor-agnostic DECT processing software.

Methods: **Phantom Construction:** An ovoid cylinder of polyurethane rubber was cast to construct a phantom mimicking the adult human abdominal environment with approximate water attenuation. The phantom consisted of three identical parts, designated Part 1, Part 2, and Part 3, with cross-section 30 cm by 22 cm and depth 18 cm. Twelve cylindrical slots were made in the cross-sectional face of each phantom part accommodating twelve polypropylene 50mL self-standing centrifuge tubes (Corning Science Mexico S.A. de C.V., ref. 430897). Each slot was loaded with one of 80 tubes containing 50mL of deionized water, lard, canola oil, a single contrast material, or a mixture of two contrast materials (**Table 1**). Tubes slots were arranged as far apart as possible within the phantom to minimize the effects of scatter during scanning (**Figure 1**). Tubes were placed in the phantom parts in 3 batches, scanned as Setup 1, Setup 2, and Setup 3. The first 36 tubes were loaded into Parts 1-3 of the phantom in numerical order. This phantom setup was designated and scanned as Setup 1. The tubes in Parts 2 and 3 were removed and tubes 37 through 56 were loaded in numerical order. This revised setup of Part 2 and Part 3 was scanned separately as Setup 2. Setup 3 consisted of phantom Parts 2 and 3 containing tubes 57 through 80.

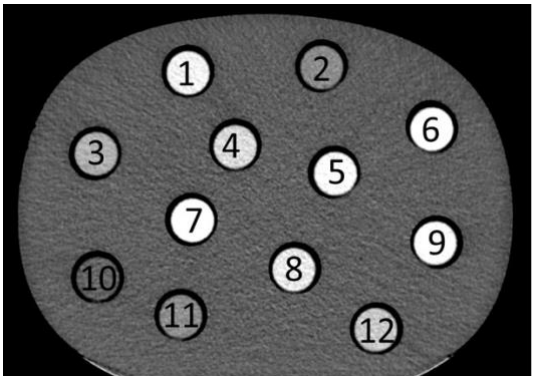

Figure 1. 120 kVp axial reconstruction of phantom Setup 1 Part 1, showing the arrangement of tubes in numbered

Table 1. Summary of tube contents, position in phantom, and expected HU at 120 kVp

Tube Number	Contents	Expected HU at 120 kVp	Phantom Position (part-slot)	Tube Number	Contents	Expected HU at 120 kVp	Phantom Position (part-slot)
1	80%I	240	1-01	41	60%I	180	2-05
2	20%I	60	1-02	42	40%W, 20%Ca	180	2-06
3	40%I	120	1-03	43	10%W, 10%Ca	60	2-07
4	60%W	180	1-04	44	60%W, 40%Ca	300	2-08
5	80%W	240	1-05	45	20%W, 20%Ca	120	2-09
6	100%I	300	1-06	46	40%W, 60%Ca	300	2-10
7	100%W	300	1-07	47	H2O	0	2-12
8	80%Ca	240	1-08	48	H2O	0	3-01
9	100%Ca	300	1-09	49	NX9		3-02
10	H2O	0	1-10	50	20%W, 80%Ca	300	3-03
11	20%W	60	1-11	51	20%W, 40%Ca	180	3-04
12	60%Ca	180	1-12	52	40%W, 40%Ca	240	3-05
13	80%I, 20%Ca	300	2-01	53	60%W, 20%Ca	240	3-06
14	10%I, 10%W	60	2-02	54	20%W, 60%Ca	240	3-07
15	60%I, 20%W	240	2-03	55	Canola oil		3-08
16	20%I, 20%W	120	2-04	56	40%Ca	120	3-09
17	20%I, 40%W	180	2-05	57	15% NX9		2-01
18	20%I, 60%W	240	2-06	58	40% Tungsten	120	2-02
19	40%I, 60%W	300	2-07	59	10 mg/mL Neodymium		2-03
20	40%I, 40%W	240	2-08	60	100% Iodine	300	2-04
21	60%I, 40%W	300	2-09	61	6% NX9		2-05
22	80%I, 20%W	300	2-10	62	20 mg/mL Neodymium		2-06
23	40%I, 20%W	180	2-11	63	15 mg/mL Neodymium		2-07
24	H2O	0	2-12	64	100% Calcium	300	2-08

Vial Number	Contents	Expected HU at 120 kVp	Phantom Position (part-slot)	Vial Number	Contents	Expected HU at 120 kVp	Phantom Position (part-slot)
25	60%I, 20%Ca	240	3-01	65	H2O	0	2-09
26	40%I, 40%Ca	240	3-02	66	5 mg/mL Tantalum		2-10
27	20%I, 20%Ca	120	3-03	67	12% NX9		2-11
28	20%I, 80%Ca	300	3-04	68	100% Tungsten	300	2-12
29	60%I, 40%Ca	300	3-05	69	20% Calcium	60	3-01
30	40%I, 20%Ca	180	3-06	70	15 mg/mL Tantalum		3-02
31	20%I, 40%Ca	180	3-07	71	10 mg/mL Tantalum		3-03
32	20%I, 60%Ca	240	3-08	72	9% NX9		3-04
33	40%I, 60%Ca	300	3-09	73	40% Calcium	120	3-05
34	10%I, 10%C	60	3-10	74	40% Iodine	120	3-06
35	20%Ca	60	3-11	75	15 mg/mL Iodine	375	3-07
36	Lard		3-12	76	20% Tungsten	60	3-08
37	NX9		2-01	77	10 mg/mL Iodine	250	3-09
38	40%W	120	2-02	78	3% NX9		3-10
39	20%I, 80%W	300	2-03	79	20 mg/mL Iodine	500	3-11
40	80%W, 20%Ca	300	2-04	80	20 mg/mL Tantalum		3-12

Contrast Solutions Preparation: Contrast materials were prepared as aqueous solutions of iodine (Omnipaque iohexol injection, GE Healthcare, NDC 0407-1414-91), calcium (calcium chloride dihydrate, Research Products International, Mt. Prospect, IL 60056 USA), tungsten (sodium tungstate dihydrate, Sigma Aldrich, ACS reagent, ≥99%), and an experimental CT contrast agent NX9. Stock solutions of iodine, calcium,

and tungsten were prepared such that each appeared as 300 HU at 120 kVp. Stock solutions consisted of 12.6 mg/mL iodine, 56.17 mg/mL calcium, and 11.17 mg/mL tungsten. The attenuation of each of these stock solutions was confirmed to be 300 HU at 120 kVp as scanned using the General Electric Discovery CT 750HD. Xanthan gum was added to stock solutions of calcium and tungsten in order to hold the particulate materials in suspension. Three hundred HU was arbitrarily chosen as a target value that allows easy observation of positive or negative fluctuations in HU with different scan/reconstruction parameters without causing excessive streak artifact. Stock solutions were designated as “100%” material solutions and dilutions were performed to produce 20%, 40%, 60%, and 80% solutions of each contrast material. Tubes containing water were used to represent the 0% solution of any contrast material in analyses. Additionally, solutions of 10, 15, and 20 mg/mL iodine were included in Setup 3. Aqueous solutions of tantalum and neodymium were provided by General Electric Medical Systems. Solutions of 5, 10, 15, and 20 mg/mL tantalum were made. Solutions of 10, 15, and 20 mg/mL neodymium were made. The experimental contrast agent, NX9, contains a negatively attenuating, low-density microparticle of composition that is proprietary to the developer Nextrast, Inc. at the time of this study. The NX9 particles used in Setup 2 had a density 30% greater than that of those used in Setup 3. The lower density NX9 particles in Setup 3 were formulated in concentrations of 3, 6, 9, 12, and 15 percent of solution by weight.

Phantom Scans: Phantom scans were performed at University of California, San Francisco, Zuckerberg San Francisco General Hospital, and San Francisco Veterans Affairs Medical Center with 6 DECT systems in clinical use: Siemens Somatom

Definition Edge (Edge), Siemens Somatom Definition Flash (Flash), Siemens Somatom Definition Force (Force), Philips IQon Spectral CT (IQon), General Electric Discovery CT 750HD (Discovery), General Electric Revolution CT (Revolution), and Canon Aquilion ONE GENESIS 640 (Canon). Acquisition parameters were kept as similar as possible given the variation of design and technical specifications between systems (Table 1), and CTDIvol was set to 30 $\pm$ 4 mGy. Images were acquired from the minimum to maximum kVp in intervals of 20 kVp on each system, and axial VMI were reconstructed from the minimum to maximum keV in intervals of 5 keV. Phantom Setups 1 and 2 were scanned separately on each system in the same orientation. Phantom parts were placed in numerical order as close together as possible on the table, with tube caps oriented outward of the scanner, and the scan beginning with Part 3. For logistic reasons, Setup 3 was scanned only on the IQon, Revolution, and Discovery systems. To assess the effects of position within the phantom on tube attenuation, Setup 3 was scanned on the Discovery scanner with the original tube arrangement as in Table 1 as well as in a scrambled setup, where the positions of 3 tube pairs were switched: 57 and 63, 61 and 68, and 69 and 75. These alternate tube positions were used to assess the effect of deep vs superficial positioning within the phantom of 100% tungsten, 15 mg/mL iodine, and 15% NX9 tubes. To assess the effect of possible phantom inhomogeneity, phantom Parts 1, 2, and 3 were also scanned on the Discovery system with only a single tube in each phantom part (15% NX9, 20 mg/mL iodine, 20 mg/mL tantalum). Each tube was positioned in slot 8 of a phantom part.

Table 2. Summary of scanner specifications and phantom scan parameters

	Scanner					
Parameter	Edge	Flash	Force	Iqon	Revolution	Discovery
Tube voltage gap (kV, low/high)	120	80/140, 100/140	80/150, 100/150	80/140	70/140	80/140
Tube current (mA)	504	582/224, 290/224	126/78, 147/75	406	200	200
Field of view (cm)	50	50	50	50	50	50
Gantry revolution time (sec)	0.28	0.33	0.285	0.5	0.35	0.25
Acquisition mode	Single source	Dual source	Dual source	Single source	Single source	Single source
Slice thickness (mm)	2	2	2	2	1.25	1.25
Slice gap (mm)	-	-	-	2	1.25	1.25
Matrix	512 x 512	512 x 512	512 x 512	512 x 512	512 x 512	512 x 512
Matrix size (mm)	312 x 312	314 x 314	350 x 350	350 x 350	350 x 350	360 x 360
Convolution kernel	I30f/3	I30f/3	Br40d/3	B	Standard	Standard
Filter	Sn, Au	WEDGE_3 (Sn/Ti)	SN_D3 (Sn/Ti)	B	Body filter	Body filter
Source to Detector Distance (cm)	108.56	108.56	108.56	104	109.76	94.67
Source to Patient Distance (cm)	59.5	59.5	59.5	57	62.56	53.85

Image Analysis: The average HU of each vial in each image reconstruction was semi-automatically measured using the image processing software ImageJ. Ten circular regions of interest (ROI) were manually placed within each vial of one reconstruction of Setup 1 and 2 from each scanner system, taking care to avoid air bubbles and obvious regions of signal inhomogeneity as well as to distribute the ROI's along the length of the tube as much as possible. A macro was employed to record the average HU of each ROI in all image reconstructions from a given scanner. The 10 ROI measurements of each vial were then averaged to represent the average HU in each vial. Data visualization and curve fitting was performed using the statistical software R Studio.

Additional virtual monoenergetic images were reconstructed using a prototype vendor-agnostic dual energy processing software called Vitrea in development by Vital Images, Inc. (Minnetonka, MN 55343). With the unavailability of raw sinogram scan data, the 55 and 70 keV monoenergetic images were used as source images to generate third-party virtual monoenergetic images in Vitrea. Images of 55 and 70 keV were chosen as source images for Vitrea as they best approximate the 80 and 140 kVp dual energy source data commonly used in DECT systems. Iodine maps quantification maps were also generated using the Vitrea software in addition to the vendor-specific iodine maps. The attenuation profiles generated by this third-party software were compared to those generated by the vendor-specific, "native," software.

Results: **Polychromatic Images:** A summary of expected and measured HU for select concentrations of iodine, calcium, and tungsten at 120 kVp is presented in **Table 3**. These results reflect the spectral imaging performance of DECT systems for which 120 kVp data was collected: Philips IQon, GE Revolution, GE Discovery. In polychromatic

images of iodine, calcium, and tungsten solutions, HU appears linearly related to material concentration on all scanners with strong linear correlation, R^2 greater than 0.97 (**Figure 2**). In general, intersystem variation in HU also appears to increase with material concentration.

Table 3. Expected vs Measured HU at 120 kVp

Tube Contents	Attenuation at 120 kVp (HU)			
	Expected	Philips IQon	GE Revolution	GE Discovery
10 mg/mL Iodine	250	285.6	245.7	251.1
15 mg/mL Iodine	375	425.7	379	375
20 mg/mL Iodine	500	540.4	488.6	493.5
20% Calcium	60	40.1	51.1	54.8
60% Calcium	180	172.8	146.8	157.5
100% Calcium	300	281.2	248.5	260.4
20% Tungsten	60	65.8	63.45	68.7
60% Tungsten	180	191.3	177.5	170
100% Tungsten	300	320.7	304.9	283.4

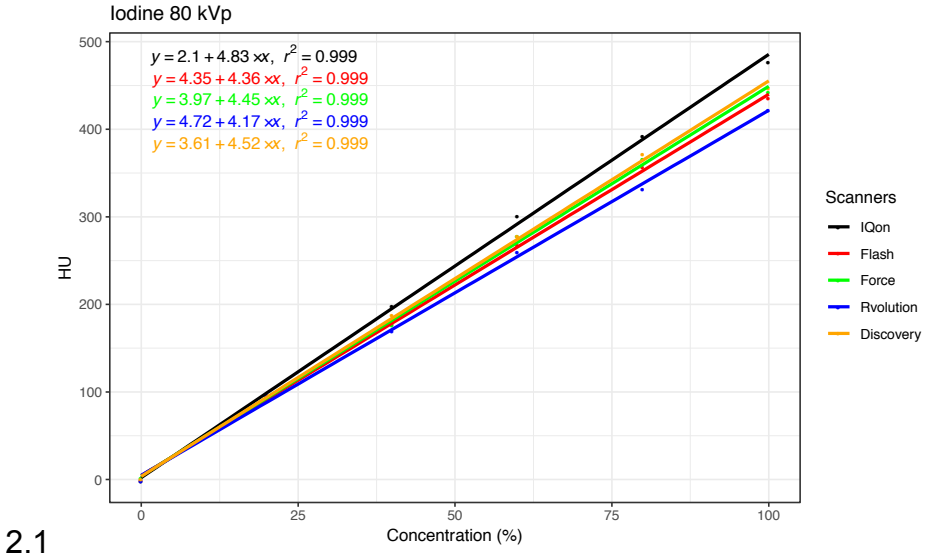

2.1

2.2

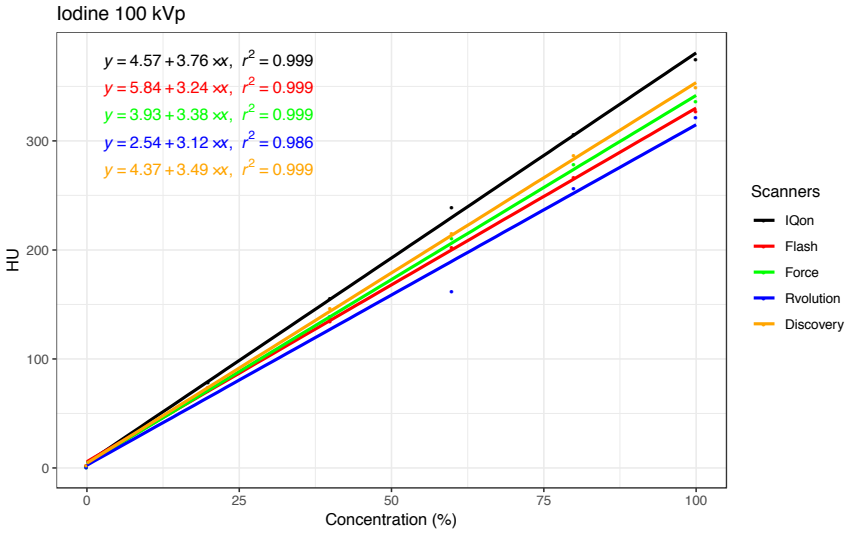

2.3

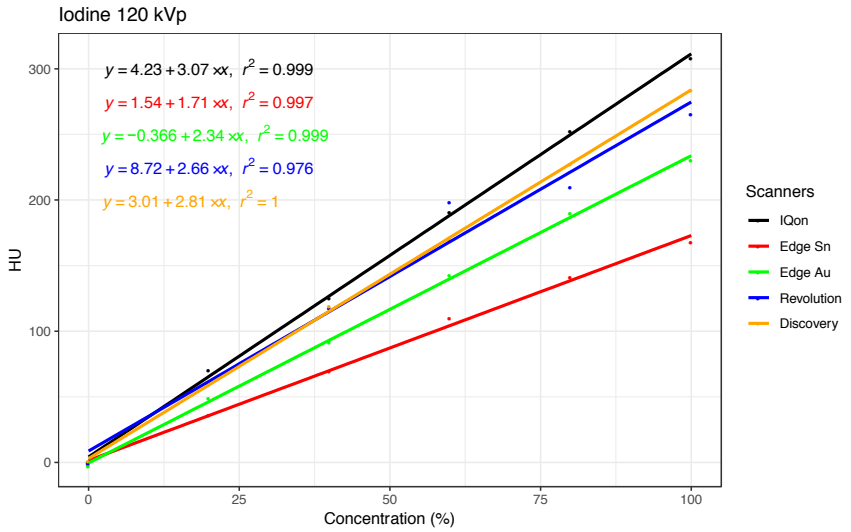

2.4

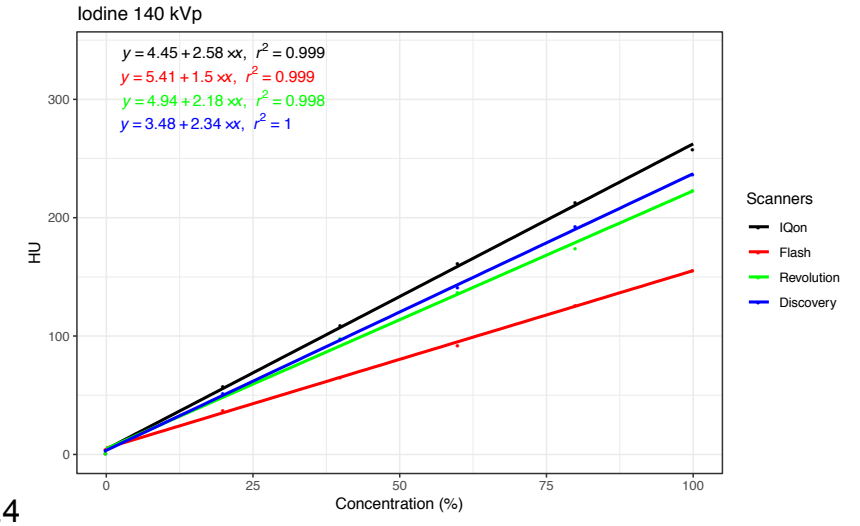

Figure 2. HU vs Concentration of iodine polychromatic reconstructions by scanner

Similar behavior is seen in the HU vs Concentration plots of polychromatic images of calcium and tungsten, with tungsten exhibiting notably less variation in HU between scanners (**Figure 3**).

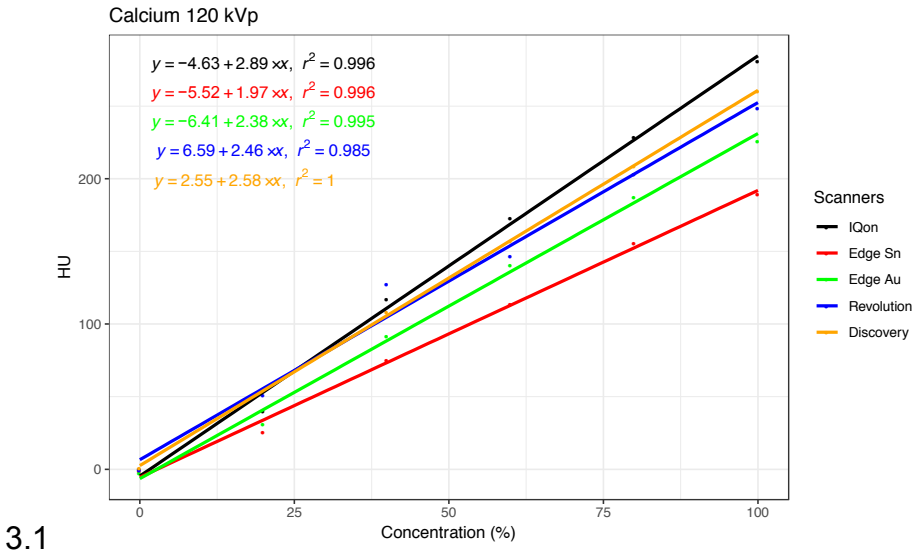

3.1

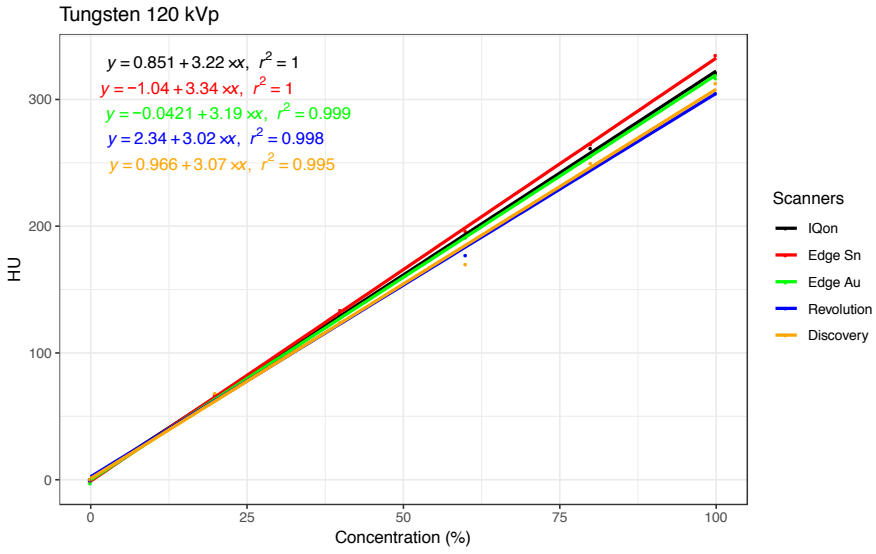

3.2

Figure 3. HU vs Concentration of calcium and tungsten polychromatic reconstructions by scanner

Monoenergetic Images: For all materials except tungsten, monoenergetic image reconstructions from all scanners show that conspicuity of all concentrations of contrast material increases with decreasing energy of reconstruction, with HU following a

second-degree exponential decay with increasing monoenergetic kilovoltage (**Figure 4**). All scanners produced similar exponential curves for all material concentrations except tungsten, which showed positive exponential behavior on the Philips IQon and Siemens Edge scanners (**Figure 4**).

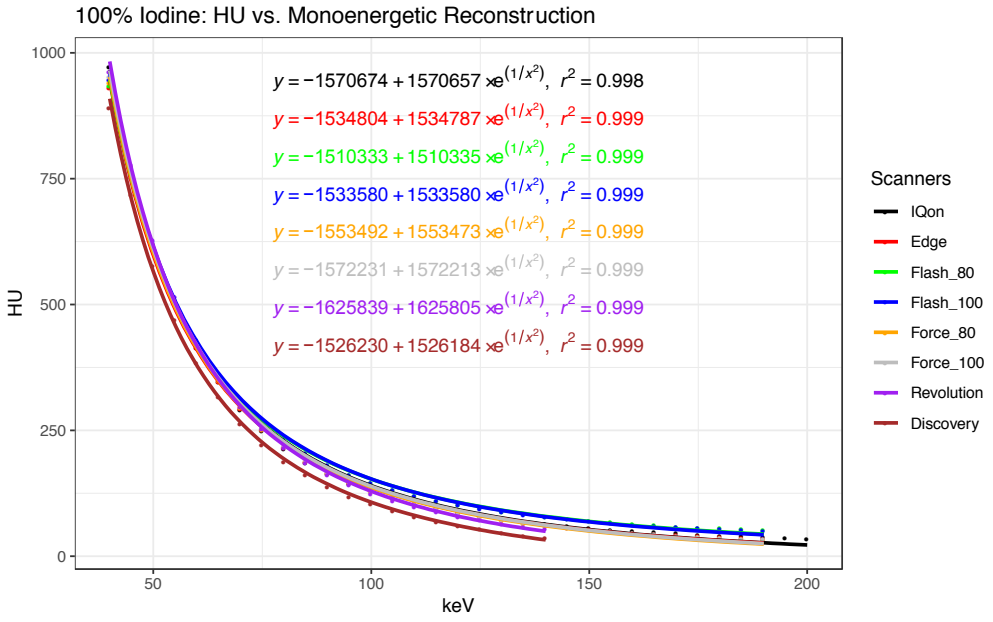

4.1

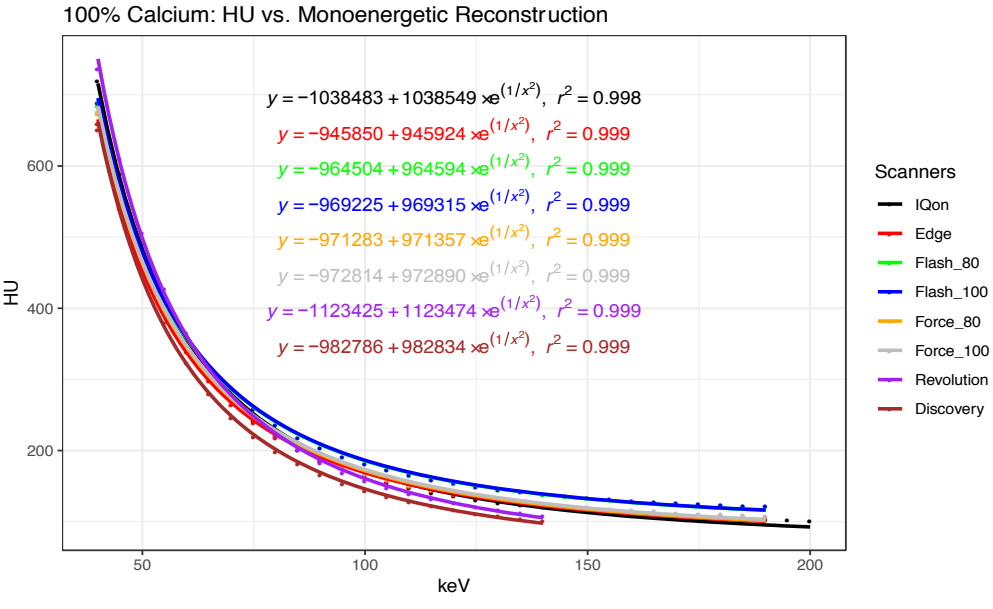

4.2

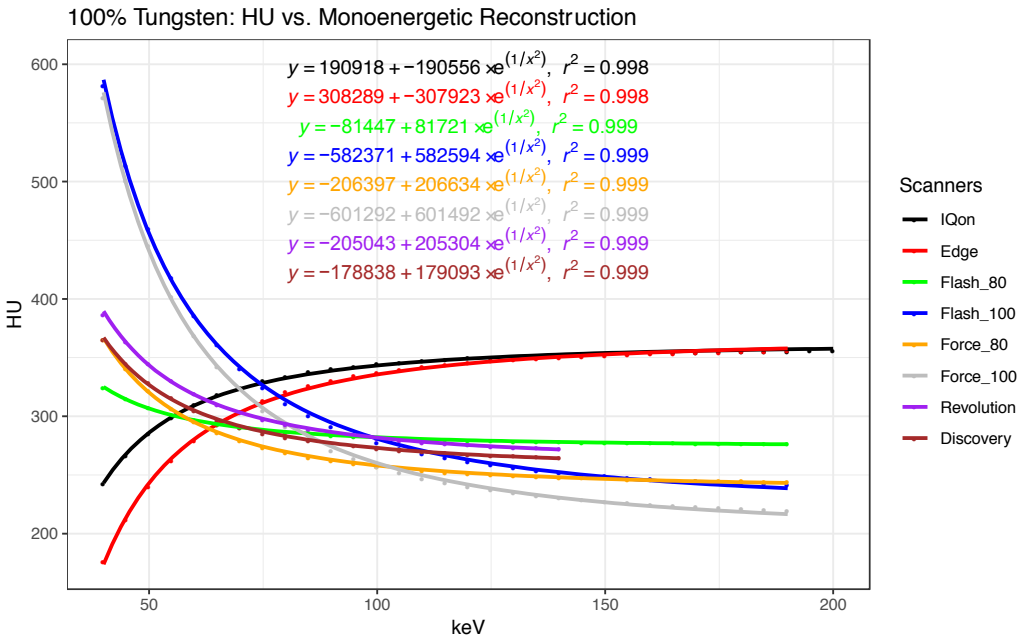

4.3

Figure 4. HU vs monoenergetic reconstruction of 100% iodine, calcium, and tungsten

The R-squared values of all curves fitted to HU vs. monoenergetic reconstruction energy plots were greater than 0.97. As a result, 95% confidence intervals are not visible on the plotted data. The equations describing HU vs. monoenergetic reconstruction energy are of the form y = A + B*e^(1/x^2), where A and B are constants unique to each curve. Constants corresponding to the native and Vitrea-generated monoenergetic curves in **Figure 5** are reported in **Table 4** (see Appendix, **Figure 10**, for monoenergetic plots of other material concentrations). Linear plots of tungsten and tantalum attenuation have only a single constant A.

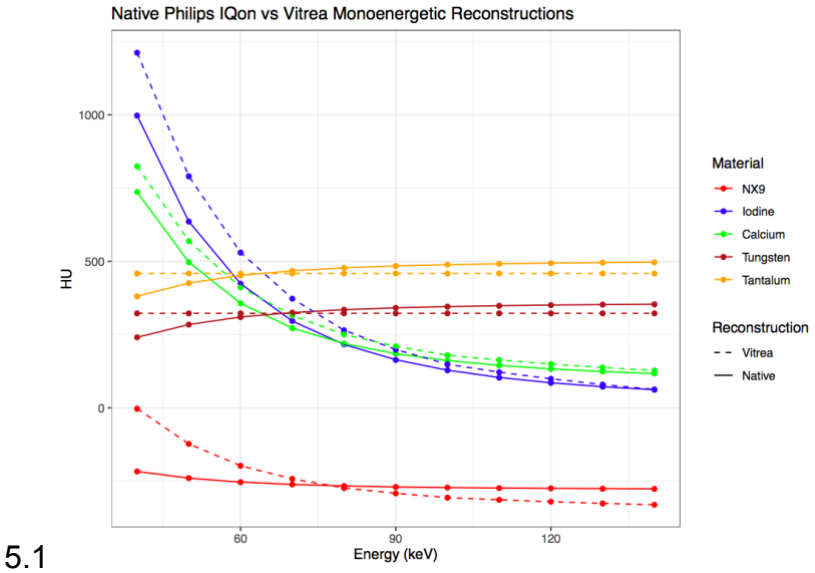

5.1

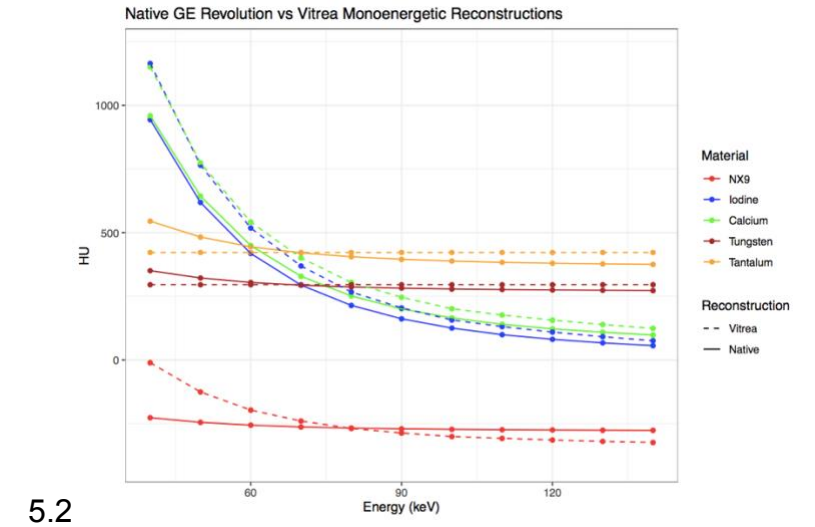

5.2

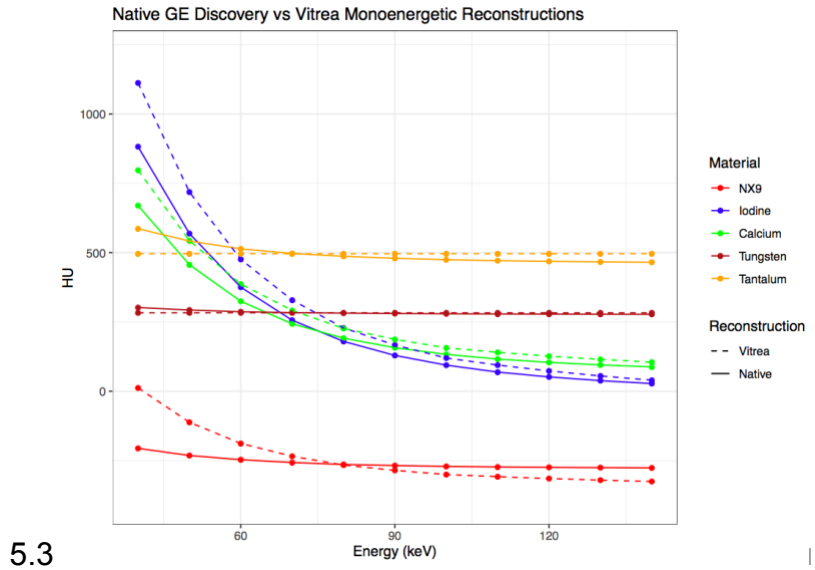

5.3

Figure 5. Native vs Vitrea monoenergetic attenuation curves by scanner

Table 4. Native vs Vitrea monoenergetic attenuation curves constants

Constant	Reconstruction					
	IQon Native	IQon Vitrea	Revolution Native	Revolution Vitrea	Discovery Native	Discovery Vitrea
NX9.1 A	-104698	-580504	-87932	-554381	-125193	-597020
NX9.1 B	104415	580143	87651	554028	124911	-597020
100% Iodine A	-1647809	-2032821	-1572435	-1926130	-1512342	-1895779
100% Iodine B	1647776	2032777	1572407	1926104	1512289	1895719
100% Calcium A	-1090702	-1232638	-1524832	-1815207	-1029952	-1223980
100% Calcium B	1090757	1232701	1524849	1815236	1029985	1224020
100% Tungsten A	199330	322.4826	-137695	295.5768	-42891	282.861
100% Tungsten B	-198965	NA	43166	NA	43166	NA
20 mg/mL Tantalum A	204834	458.2761	-300581	422.1256	-213758	495.993
20 mg/mL Tantalum B	-204325	NA	300940	NA	214211	NA

Discussion: **Polychromatic Images:** Comparison of expected vs. measured HU of iodine, calcium, and tungsten at 120 kVp across the Philips and GE DECT systems demonstrates inconsistency between systems. Both GE systems produced near-expected HU values for iodine with greater accuracy than Philips, but performed no better or worse than Philips in achieving expected HU values for calcium and tungsten. HU vs Concentration plots of materials by scanner further demonstrate differences in performance of the various scanner systems.

Limitations: Analysis was based on a single size phantom. Different sized mass-attenuators could result in deviations of the observed HU values. Furthermore, this particular phantom series is limited by a small number of missing data points. These

consisted of a few clear outliers which were intentionally omitted and certain monoenergetic reconstructions which, for logistic reasons, could not be recovered. Image series are missing for the Siemens Force 150 keV (energy gap 80/150 kVp) and 70 keV (energy gap 100/150 kVp) reconstructions of Setup 1, as well as the 155 keV (100/150 kVp) and Part 3 of the 150 keV (100/150 kVp) monoenergetic reconstructions of Setup 2. Likewise, Setup 3 could only be scanned using the Philips IQon and GE Revolution and Discovery systems for logistic reasons, only phantom Setup 1 was scanned on the Canon system. Inhomogeneity and small air bubbles suspended in the phantom tubes may also contribute to the inherent variability in the data as well as the presence of outliers.

Streak artifacts from relatively high-density tubes may affect the measured attenuation of other nearby tubes. The neighborhood and position within the phantom of a given tube may be factors contributing to its measured attenuation in addition to its contents. In the alternate tube arrangement of Setup 3, scanned on the GE Discovery system, the effect on measured attenuation of deep vs superficial tube placement within the phantom was assessed for 3 tubes: 100% tungsten, 15 mg/mL iodine, and 15% NX9. The differences in HU values at 120 kVp were found to be within the standard deviation of a given tube in either position (**Table 5**). One exception is noted in the case of 15 mg/mL iodine, where the difference in HU was slightly greater than the standard deviation of HU in the superficial position. Likewise, the tubes (15% NX9, 20 mg/mL iodine, and 20 mg/mL tantalum) scanned individually in separate phantom parts showed monoenergetic attenuation profiles (**Figure 6**) with near perfect match to the same tubes scanned in phantom Setup 3.

Table 5. Difference in HU with alternate tube position

Material	Difference in Average HU between Deep and Superficial Position at 120 kVp	Standard Deviation, Deep	Standard Deviation, Superficial
100% Tungsten	6.76	19.26	16.42
15mg/mL Iodine	19.29	21.01	16.64
15% NX9	0.87	17.89	13.45

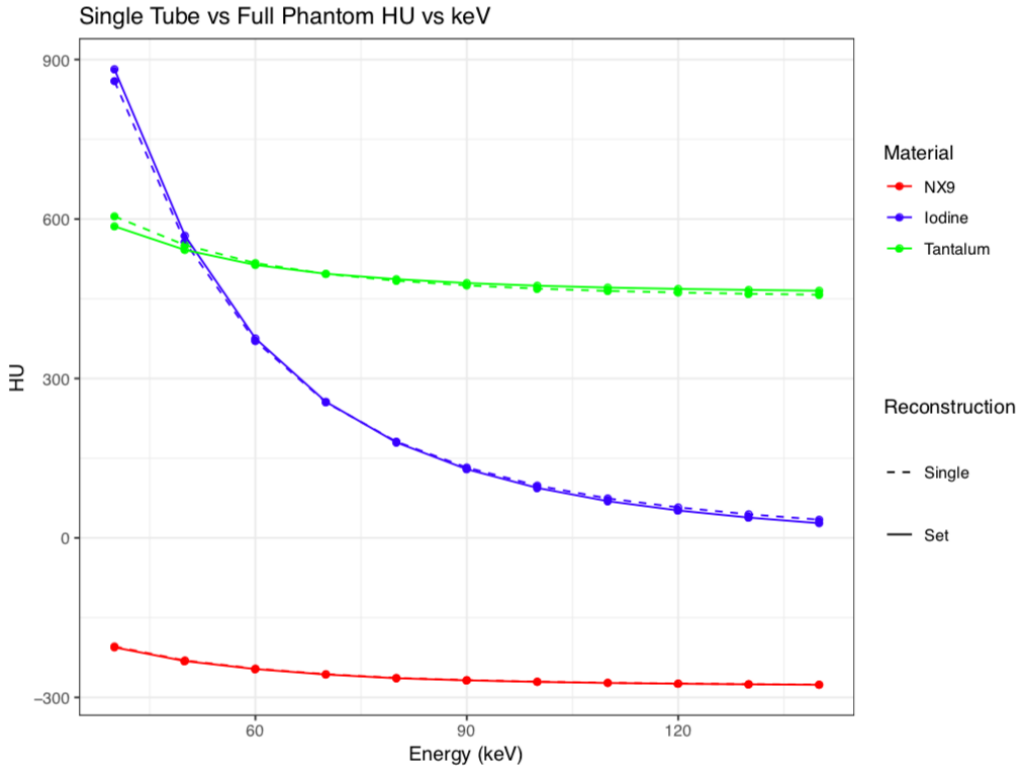

Figure 6. HU vs monoenergetic reconstruction in Single vs Full Phantom

Monoenergetic Images: All curves fitted to HU vs. monoenergetic reconstruction energy plots had near perfect fit to the plotted data, with r-squared values greater than 0.97 in all cases. Variability in local tube environment within the phantom, as a result of depth within the polyurethane phantom or possible streaking artifacts from neighboring tubes of relatively high density, was shown to have negligible effect on the HU of the

materials tested under these variable conditions. The fitted curves of HU vs. monoenergetic reconstruction can therefore be considered as good representations of the monoenergetic attenuation profiles of the materials as imaged with the specific DECT systems in question.

The 15 mg/mL tantalum tube in Setup 3 of the phantom was obtained from a stock solution which had been in storage for an extended period of time. The original concentration of tantalum may not have been preserved due to evaporation, resulting in inaccurate dilution. For this reason, the 15 mg/mL tantalum tube was excluded from analysis. A limited supply of tantalum precluded the replacement of the 15 mg/mL tantalum solution. All other dilutions of tantalum were obtained from a different stock solution and appeared to be of the correct concentration.

The GE Revolution and Siemens Force (100, 150 kVp) monoenergetic HU values of tungsten appear more closely related to one another than to those of the other scanners, especially at low extreme of monoenergetic reconstruction. Similarly, the Philips IQon and Siemens Edge monoenergetic HU values of tungsten appear to share a horizontal asymptote, with the two curves nearly coincidental from 130 keV and above. As opposed to the relative uniformity of polychromatic attenuation plots of tungsten, monoenergetic reconstructions of tungsten appeared to produce the greatest intersystem variation.

Comparison of native vs Vitrea monoenergetic reconstructions of various materials scanned on the same DECT system (**Figure 5**) show that the Vitrea reconstructions approximate the native attenuation profiles. The Vitrea NX9 curves have a steeper vertical asymptote than their native counterparts. Of note, the Vitrea-

generated monoenergetic attenuation profiles of high-z materials tungsten and tantalum are transformed from a native exponential curve to be perfectly linear on all scanners except the Siemens Edge and Force. Comparison of the native vs Vitrea monoenergetic reconstructions of the same material across different DECT systems (**Figure 7**) shows that Vitrea is able to resolve some degree of disparity in the attenuation profiles generated by different systems for tungsten and NX9, though not so for iodine and calcium.

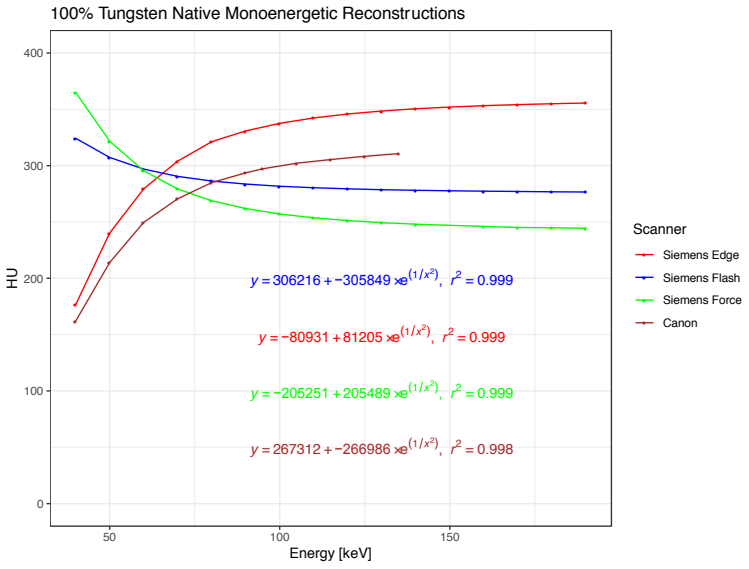

7.1

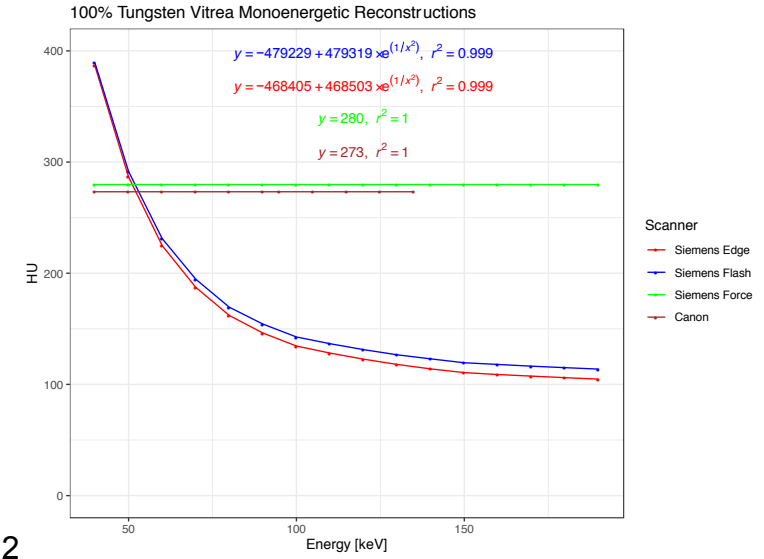

7.2

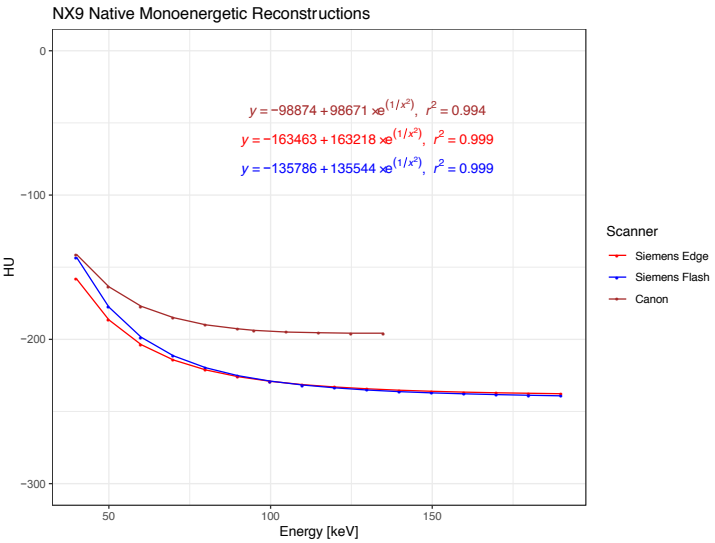
NX9 Native Monoenergetic Reconstructions
y = −98874 + 98671 xe^(1/x²), r² = 0.994
y = −163463 + 163218 xe^(1/x²), r² = 0.999
y = −135786 + 135544 xe^(1/x²), r² = 0.999
HU
0
−100
−200
−300
50
100
150
Energy [keV]
Scanner
Siemens Edge
Siemens Flash
Canon

7.3

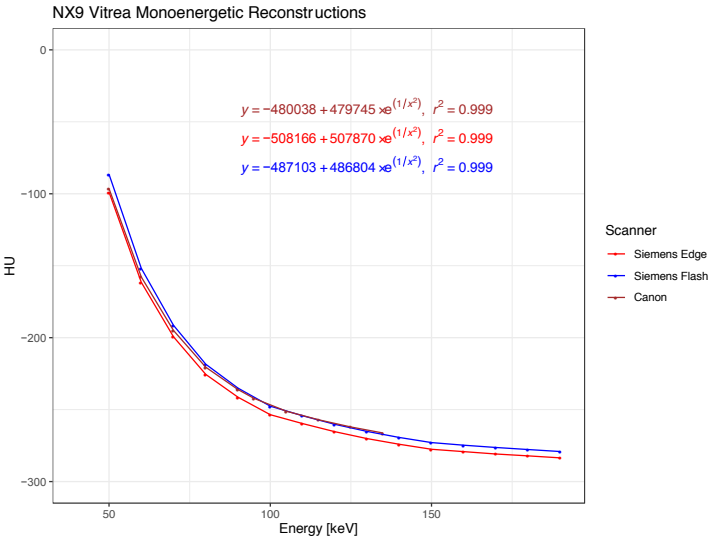
NX9 Vitrea Monoenergetic Reconstructions
y = −480038 + 479745 xe^(1/x²), r² = 0.999
y = −508166 + 507870 xe^(1/x²), r² = 0.999
y = −487103 + 486804 xe^(1/x²), r² = 0.999
HU
0
−100
−200
−300
50
100
150
Energy [keV]
Scanner
Siemens Edge
Siemens Flash
Canon

7.4

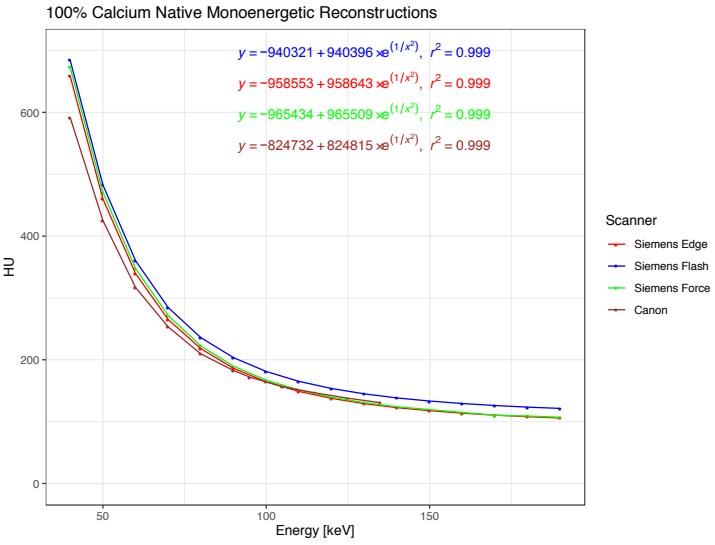
100% Calcium Native Monoenergetic Reconstructions
y = −940321 + 940396 xe^(1/x²), r² = 0.999
y = −958553 + 958643 xe^(1/x²), r² = 0.999
y = −965434 + 965509 xe^(1/x²), r² = 0.999
y = −824732 + 824815 xe^(1/x²), r² = 0.999
HU
600
400
200
0
50
100
150
Energy [keV]
Scanner
Siemens Edge
Siemens Flash
Siemens Force
Canon

7.5

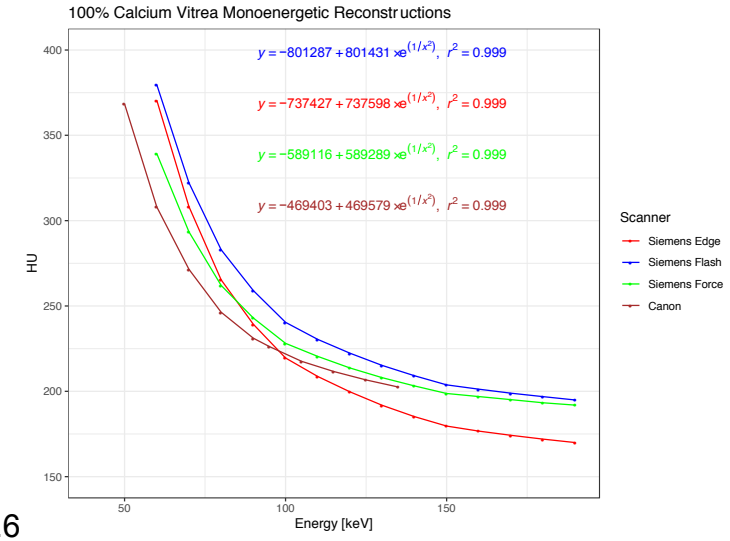

7.6

Figure 7. Native vs Vitrea monoenergetic attenuation curves by material

The plotted Vitrea-generated iodine quantification maps for the Discovery and Revolution scanners across iodine concentrations had a y-intercept and slope greater than that of the natively generated plot (**Figure 8**). The strong correlation between the iodine concentration vs attenuation profile of the two scanners is maintained, and the greater slope of the Vitrea-generated plots suggests that greater contrast and thereby easier quantification of iodine concentration may be achieved with this third-party software.

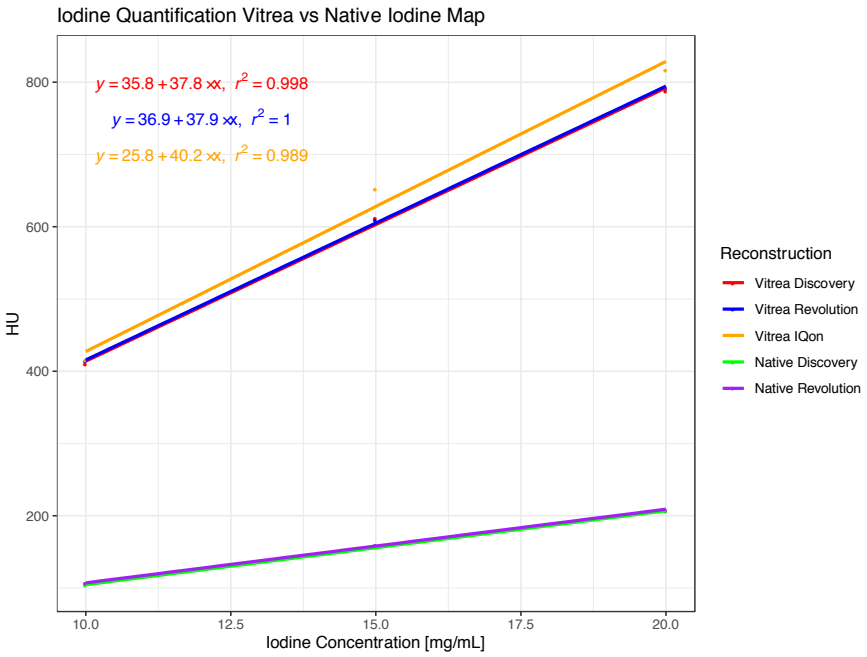

Figure 8. Native vs Vitrea iodine quantification

The method by which Vitrea generates virtual monoenergetic images and iodine maps is proprietary knowledge of Vital Images, Inc. It is unknown whether better results can be achieved when the software is used to process spectral vs monoenergetic images. At the time of this study, Vitrea software remains in development and further validation with contrast agents approved by the Food and Drug Administration is needed.

Conclusion: The results of this study affirm that there exists a general correlation of HU values between DECT scanners for most of the materials examined, but that a degree of intersystem variation in HU is present among the DECT systems examined. Despite differences between scanner systems, the attenuation profiles of the materials examined are readily differentiable. Certain materials examined in this study, such as NX9 and tantalum, may one day enter clinical use as contrast agents. A catalog of the attenuation profiles of various contrast materials scanned on the full range of clinical DECT systems can serve as a “Rosetta stone” and provide a means of translating the

HU outputs between scanners. Presently, the main focus of this project has been to describe intersystem HU variance in a variety of contrast materials. To further validate the results of this study, intersystem HU correction may be applied to in vivo multi-contrast animal DECT images.

References

1 Yu L, Leng S, McCollough CH. Dual-energy CT-based monochromatic imaging. *AJR Am J Roentgenol* 2012;**199**:S9–15.

2 Grant KL, Flohr TG, Krauss B, Sedlmair M, Thomas C, Schmidt B. Assessment of an advanced image-based technique to calculate virtual monoenergetic computed tomographic images from a dual-energy examination to improve contrast-to-noise ratio in examinations using iodinated contrast media. *Invest Radiol* 2014;**49**:586–92.

3 Bodanapally UK, Archer-Arroyo KL, Dreizin D, Shanmuganathan K, Schwartzbauer G, Li G, *et al.* Dual-Energy Computed Tomography Imaging of Head: Virtual High-Energy Monochromatic (190 keV) Images Are More Reliable Than Standard 120 kV Images for Detecting Traumatic Intracranial Hemorrhages. *Journal of Neurotrauma* 2019:1375–81. https://doi.org/10.1089/neu.2018.5985.

4 Genant HK, Boyd D. Quantitative Bone Mineral Analysis Using Dual Energy Computed Tomography. *Invest Radiol* 1977:545–51. https://doi.org/10.1097/00004424-197711000-00015.

5 Kelcz F, Joseph PM, Hilal SK. Noise considerations in dual energy CT scanning. *Med Phys* 1979;**6**:418–25.

6 Avrin DE, Macovski A, Zatz LE. Clinical application of Compton and photo-electric reconstruction in computed tomography: preliminary results. *Invest Radiol* 1978;**13**:217–22.

7 Yeh BM, Shepherd JA, Wang ZJ, Teh HS, Hartman RP, Prevrhal S. Dual-energy and low-kVp CT in the abdomen. *AJR Am J Roentgenol* 2009;**193**:47–54.

8 Johnson TRC. Dual-energy CT: general principles. *AJR Am J Roentgenol* 2012;**199**:S3–8.

9 Wortman JR, Sodickson AD. Pearls, Pitfalls, and Problems in Dual-Energy Computed Tomography Imaging of the Body. *Radiol Clin North Am* 2018;**56**:625–40.

10 Flohr T, Schmidt B. Technical Aspects of Dual Energy CT with Dual Source CT Systems. *Dual-Energy CT in Cardiovascular Imaging* 2015:11–32. https://doi.org/10.1007/978-3-319-21227-2_2.

11 Ehn S, Sellerer T, Muenzel D, Fingerle AA, Kopp F, Duda M, *et al.* Assessment of quantification accuracy and image quality of a full-body dual-layer spectral CT system. *J Appl Clin Med Phys* 2018;**19**:204–17.

12 Patino M, Prochowski A, Agrawal MD, Simeone FJ, Gupta R, Hahn PF, *et al.* Material Separation Using Dual-Energy CT: Current and Emerging Applications. *Radiographics* 2016;**36**:1087–105.

13 Toepker M, Moritz T, Krauss B, Weber M, Euller G, Mang T, *et al.* Virtual non-contrast in second-generation, dual-energy computed tomography: reliability of attenuation values. *Eur J Radiol* 2012;**81**:e398–405.

14 Coursey CA, Nelson RC, Boll DT, Paulson EK, Ho LM, Neville AM, *et al.* Dual-energy multidetector CT: how does it work, what can it tell us, and when can we use it in abdominopelvic imaging? *Radiographics* 2010;**30**:1037–55.

15 Yeh BM, FitzGerald PF, Edic PM, Lambert JW, Colborn RE, Marino ME, *et al.* Opportunities for new CT contrast agents to maximize the diagnostic potential of emerging spectral CT technologies. *Adv Drug Deliv Rev* 2017;**113**:201–22.

16 Mileto A, Barina A, Marin D, Stinnett SS, Choudhury KR, Wilson JM, *et al.* Virtual Monochromatic Images from Dual-Energy Multidetector CT: Variance in CT Numbers from the Same Lesion between Single-Source Projection-based and Dual-Source Image-based Implementations. *Radiology* 2016:269–77. https://doi.org/10.1148/radiol.2015150919.

Appendix

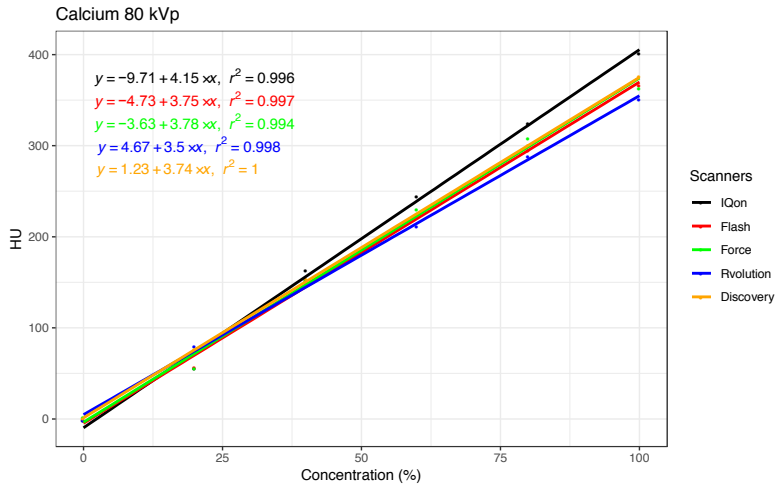

9.1

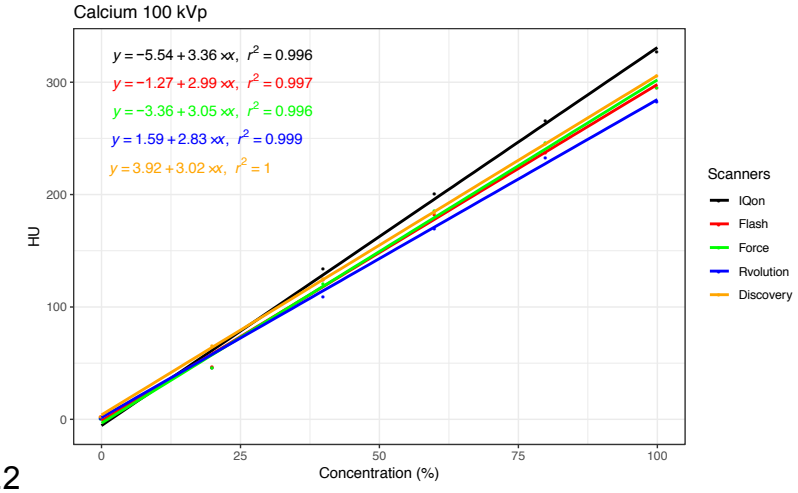

9.2

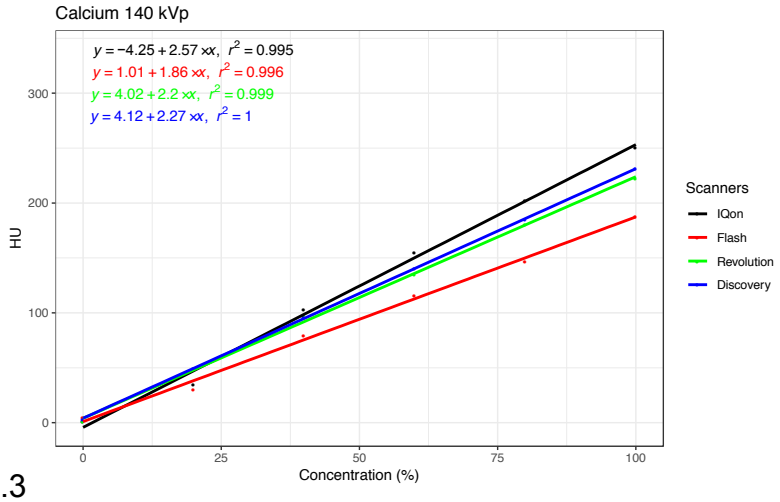

9.3

9.4

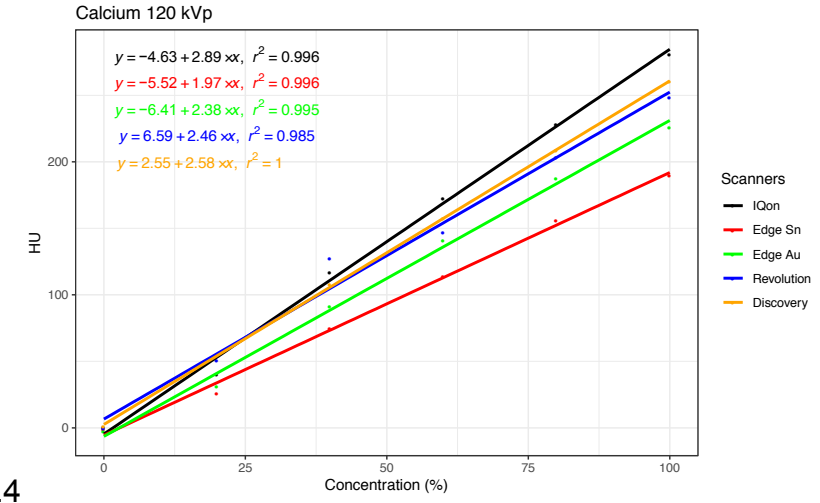
Calcium 120 kVp
y = −4.63 + 2.89 xx, r² = 0.996
y = −5.52 + 1.97 xx, r² = 0.996
y = −6.41 + 2.38 xx, r² = 0.995
y = 6.59 + 2.46 xx, r² = 0.985
y = 2.55 + 2.58 xx, r² = 1
HU
Concentration (%)
Scanners
IQon
Edge Sn
Edge Au
Revolution
Discovery

9.5

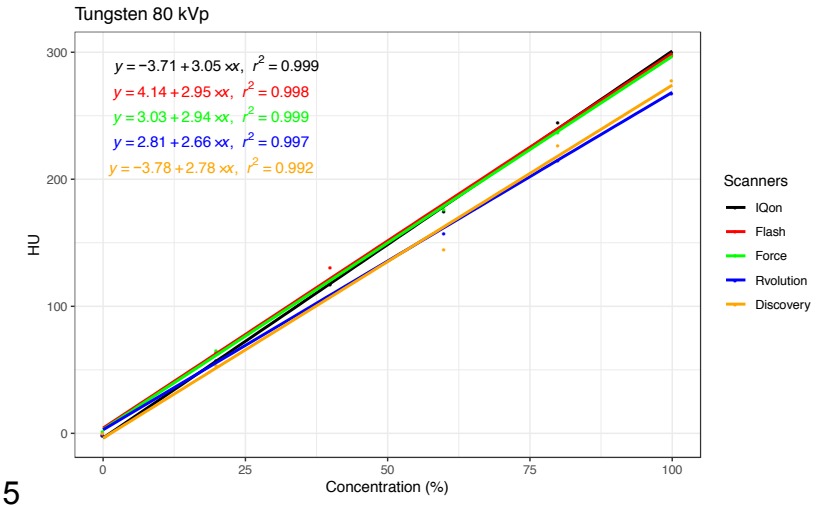
Tungsten 80 kVp
y = −3.71 + 3.05 xx, r² = 0.999
y = 4.14 + 2.95 xx, r² = 0.998
y = 3.03 + 2.94 xx, r² = 0.999
y = 2.81 + 2.66 xx, r² = 0.997
y = −3.78 + 2.78 xx, r² = 0.992
HU
Concentration (%)
Scanners
IQon
Flash
Force
Rvolution
Discovery

9.6

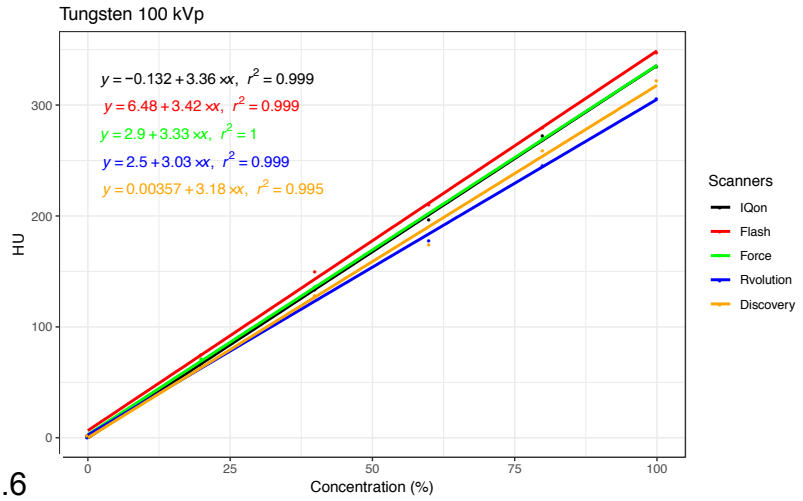
Tungsten 100 kVp
y = −0.132 + 3.36 xx, r² = 0.999
y = 6.48 + 3.42 xx, r² = 0.999
y = 2.9 + 3.33 xx, r² = 1
y = 2.5 + 3.03 xx, r² = 0.999
y = 0.00357 + 3.18 xx, r² = 0.995
HU
Concentration (%)
Scanners
IQon
Flash
Force
Rvolution
Discovery

9.7

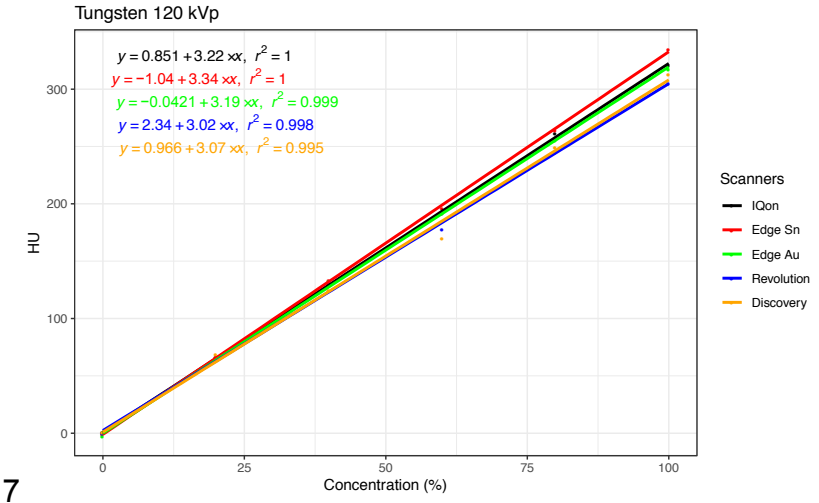

9.8

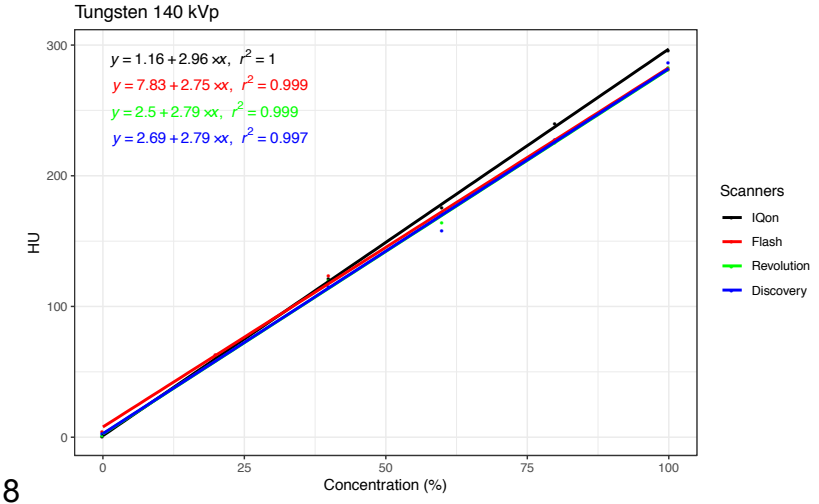

Figure 9. HU vs Concentration of calcium and tungsten by scanner

10.1

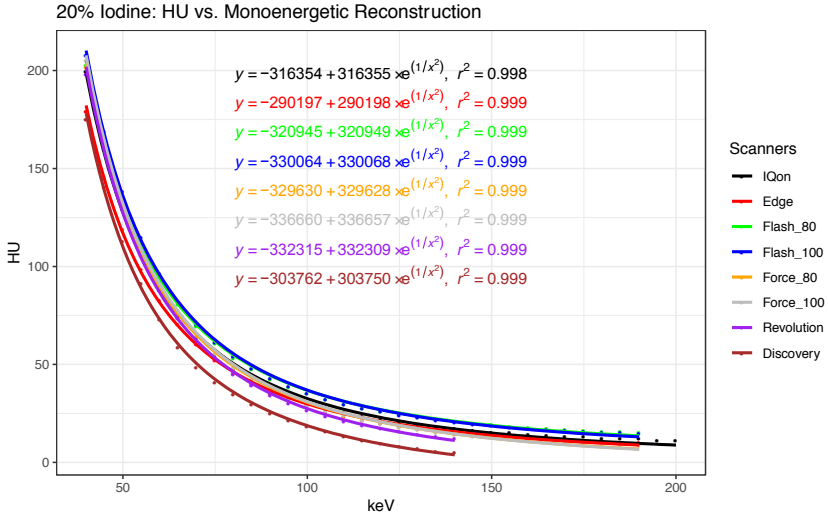

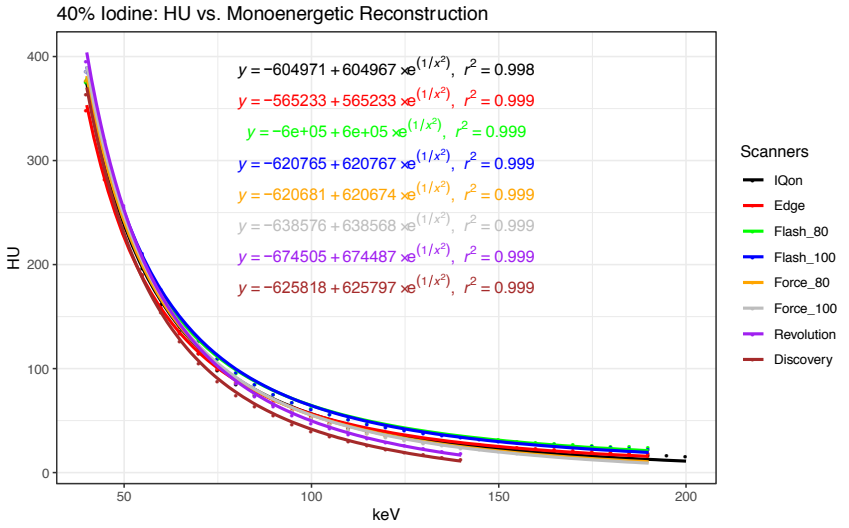
40% Iodine: HU vs. Monoenergetic Reconstruction
y = −604971 + 604967 × e^(1/x²), r² = 0.998
y = −565233 + 565233 × e^(1/x²), r² = 0.999
y = −6e+05 + 6e+05 × e^(1/x²), r² = 0.999
y = −620765 + 620767 × e^(1/x²), r² = 0.999
y = −620681 + 620674 × e^(1/x²), r² = 0.999
y = −638576 + 638568 × e^(1/x²), r² = 0.999
y = −674505 + 674487 × e^(1/x²), r² = 0.999
y = −625818 + 625797 × e^(1/x²), r² = 0.999
HU
keV
Scanners
IQon
Edge
Flash_80
Flash_100
Force_80
Force_100
Revolution
Discovery

10.2

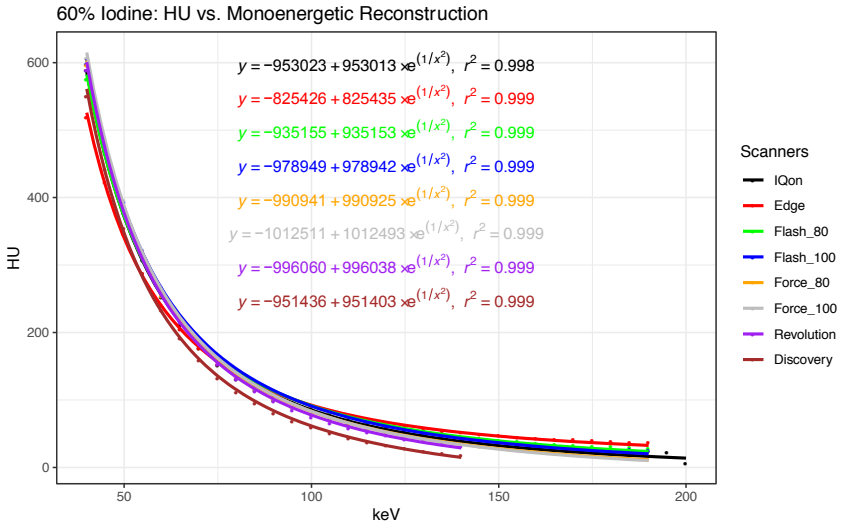
60% Iodine: HU vs. Monoenergetic Reconstruction
y = −953023 + 953013 × e^(1/x²), r² = 0.998
y = −825426 + 825435 × e^(1/x²), r² = 0.999
y = −935155 + 935153 × e^(1/x²), r² = 0.999
y = −978949 + 978942 × e^(1/x²), r² = 0.999
y = −990941 + 990925 × e^(1/x²), r² = 0.999
y = −1012511 + 1012493 × e^(1/x²), r² = 0.999
y = −996060 + 996038 × e^(1/x²), r² = 0.999
y = −951436 + 951403 × e^(1/x²), r² = 0.999
HU
keV
Scanners
IQon
Edge
Flash_80
Flash_100
Force_80
Force_100
Revolution
Discovery

10.3

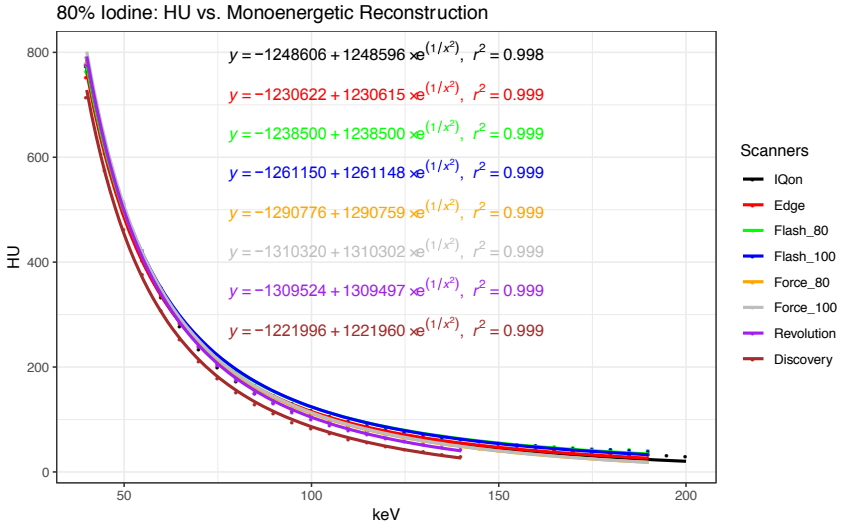
80% Iodine: HU vs. Monoenergetic Reconstruction
y = −1248606 + 1248596 × e^(1/x²), r² = 0.998
y = −1230622 + 1230615 × e^(1/x²), r² = 0.999
y = −1238500 + 1238500 × e^(1/x²), r² = 0.999
y = −1261150 + 1261148 × e^(1/x²), r² = 0.999
y = −1290776 + 1290759 × e^(1/x²), r² = 0.999
y = −1310320 + 1310302 × e^(1/x²), r² = 0.999
y = −1309524 + 1309497 × e^(1/x²), r² = 0.999
y = −1221996 + 1221960 × e^(1/x²), r² = 0.999
HU
keV
Scanners
IQon
Edge
Flash_80
Flash_100
Force_80
Force_100
Revolution
Discovery

10.4

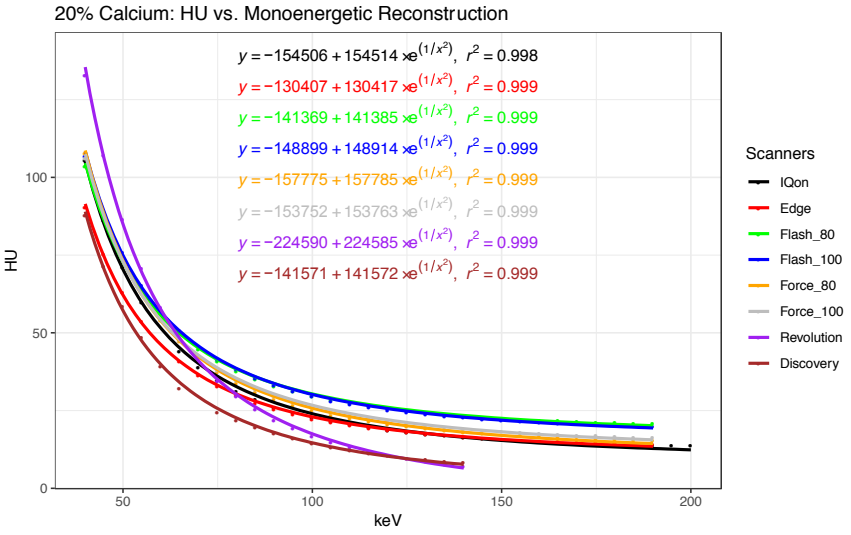
20% Calcium: HU vs. Monoenergetic Reconstruction
y = −154506 + 154514 × e^(1/x²), r² = 0.998
y = −130407 + 130417 × e^(1/x²), r² = 0.999
y = −141369 + 141385 × e^(1/x²), r² = 0.999
y = −148899 + 148914 × e^(1/x²), r² = 0.999
y = −157775 + 157785 × e^(1/x²), r² = 0.999
y = −153752 + 153763 × e^(1/x²), r² = 0.999
y = −224590 + 224585 × e^(1/x²), r² = 0.999
y = −141571 + 141572 × e^(1/x²), r² = 0.999
HU
keV
Scanners
IQon
Edge
Flash_80
Flash_100
Force_80
Force_100
Revolution
Discovery

10.5

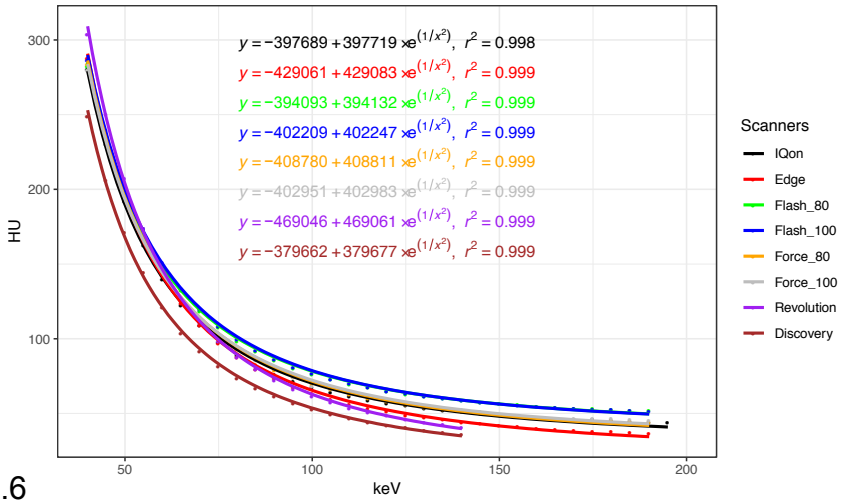
40% Calcium: HU vs. Monoenergetic Reconstruction
y = −397689 + 397719 × e^(1/x²), r² = 0.998
y = −429061 + 429083 × e^(1/x²), r² = 0.999
y = −394093 + 394132 × e^(1/x²), r² = 0.999
y = −402209 + 402247 × e^(1/x²), r² = 0.999
y = −408780 + 408811 × e^(1/x²), r² = 0.999
y = −402951 + 402983 × e^(1/x²), r² = 0.999
y = −469046 + 469061 × e^(1/x²), r² = 0.999
y = −379662 + 379677 × e^(1/x²), r² = 0.999
HU
keV
Scanners
IQon
Edge
Flash_80
Flash_100
Force_80
Force_100
Revolution
Discovery

10.6

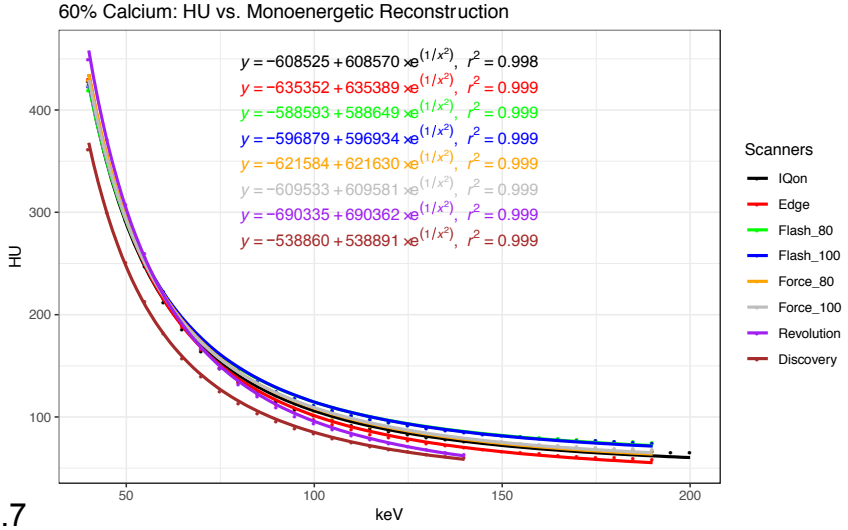
60% Calcium: HU vs. Monoenergetic Reconstruction
y = −608525 + 608570 × e^(1/x²), r² = 0.998
y = −635352 + 635389 × e^(1/x²), r² = 0.999
y = −588593 + 588649 × e^(1/x²), r² = 0.999
y = −596879 + 596934 × e^(1/x²), r² = 0.999
y = −621584 + 621630 × e^(1/x²), r² = 0.999
y = −609533 + 609581 × e^(1/x²), r² = 0.999
y = −690335 + 690362 × e^(1/x²), r² = 0.999
y = −538860 + 538891 × e^(1/x²), r² = 0.999
HU
keV
Scanners
IQon
Edge
Flash_80
Flash_100
Force_80
Force_100
Revolution
Discovery

10.7

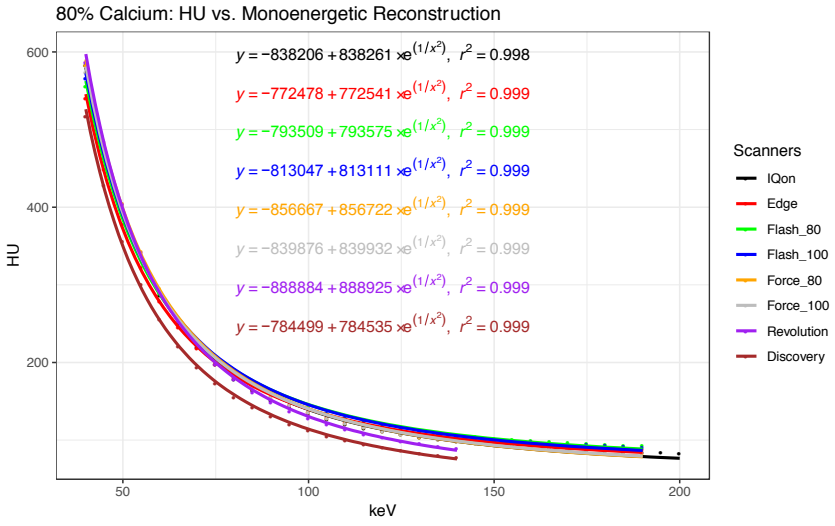
80% Calcium: HU vs. Monoenergetic Reconstruction
y = −838206 + 838261 × e^(1/x²), r² = 0.998
y = −772478 + 772541 × e^(1/x²), r² = 0.999
y = −793509 + 793575 × e^(1/x²), r² = 0.999
y = −813047 + 813111 × e^(1/x²), r² = 0.999
y = −856667 + 856722 × e^(1/x²), r² = 0.999
y = −839876 + 839932 × e^(1/x²), r² = 0.999
y = −888884 + 888925 × e^(1/x²), r² = 0.999
y = −784499 + 784535 × e^(1/x²), r² = 0.999
HU
600
400
200
50
100
150
200
keV
Scanners
IQon
Edge
Flash_80
Flash_100
Force_80
Force_100
Revolution
Discovery

10.8

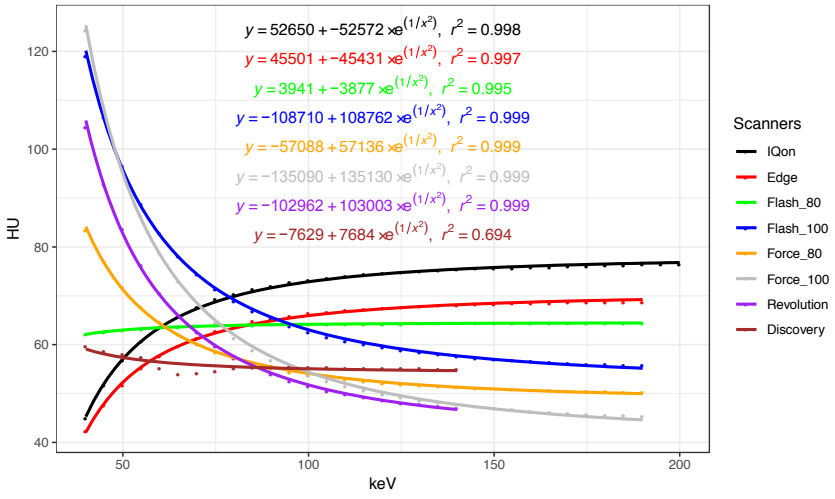
20% Tungsten: HU vs. Monoenergetic Reconstruction
y = 52650 + −52572 × e^(1/x²), r² = 0.998
y = 45501 + −45431 × e^(1/x²), r² = 0.997
y = 3941 + −3877 × e^(1/x²), r² = 0.995
y = −108710 + 108762 × e^(1/x²), r² = 0.999
y = −57088 + 57136 × e^(1/x²), r² = 0.999
y = −135090 + 135130 × e^(1/x²), r² = 0.999
y = −102962 + 103003 × e^(1/x²), r² = 0.999
y = −7629 + 7684 × e^(1/x²), r² = 0.694
HU
120
100
80
60
40
50
100
150
200
keV
Scanners
IQon
Edge
Flash_80
Flash_100
Force_80
Force_100
Revolution
Discovery

10.9

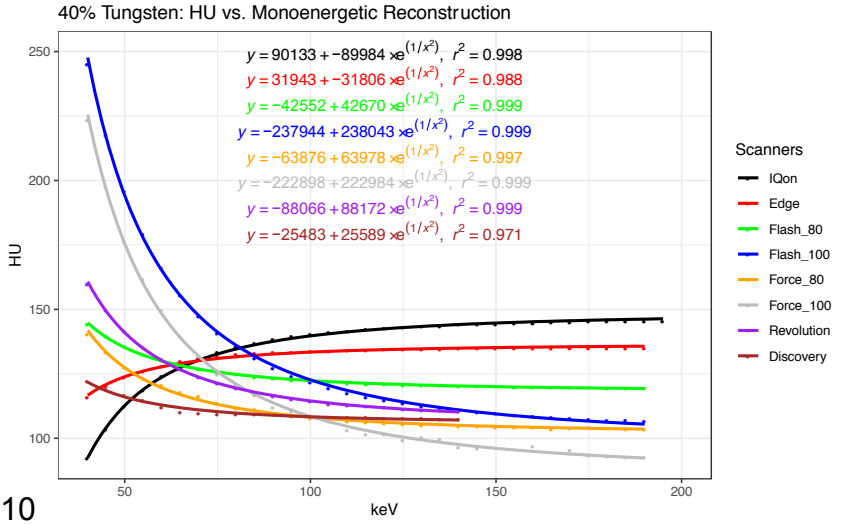
40% Tungsten: HU vs. Monoenergetic Reconstruction
y = 90133 + −89984 × e^(1/x²), r² = 0.998
y = 31943 + −31806 × e^(1/x²), r² = 0.988
y = −42552 + 42670 × e^(1/x²), r² = 0.999
y = −237944 + 238043 × e^(1/x²), r² = 0.999
y = −63876 + 63978 × e^(1/x²), r² = 0.997
y = −222898 + 222984 × e^(1/x²), r² = 0.999
y = −88066 + 88172 × e^(1/x²), r² = 0.999
y = −25483 + 25589 × e^(1/x²), r² = 0.971
HU
250
200
150
100
50
100
150
200
keV
Scanners
IQon
Edge
Flash_80
Flash_100
Force_80
Force_100
Revolution
Discovery

10.10

10.11

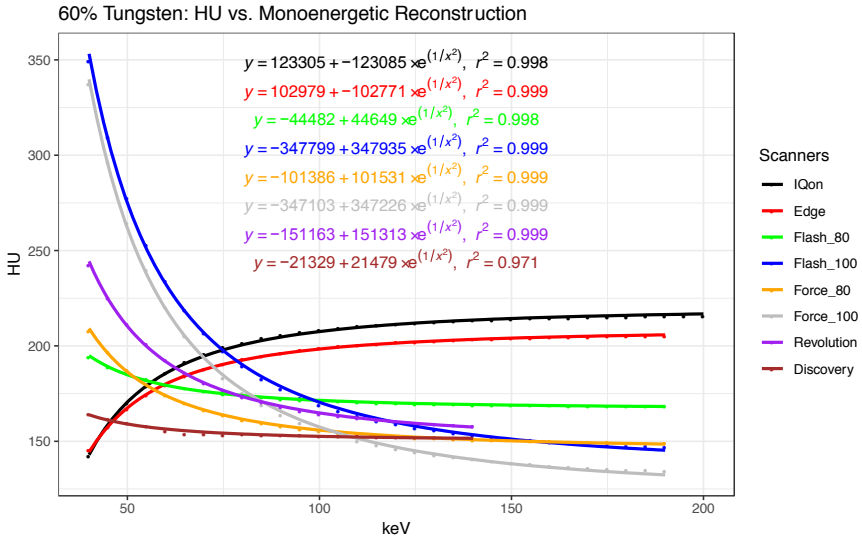

10.12

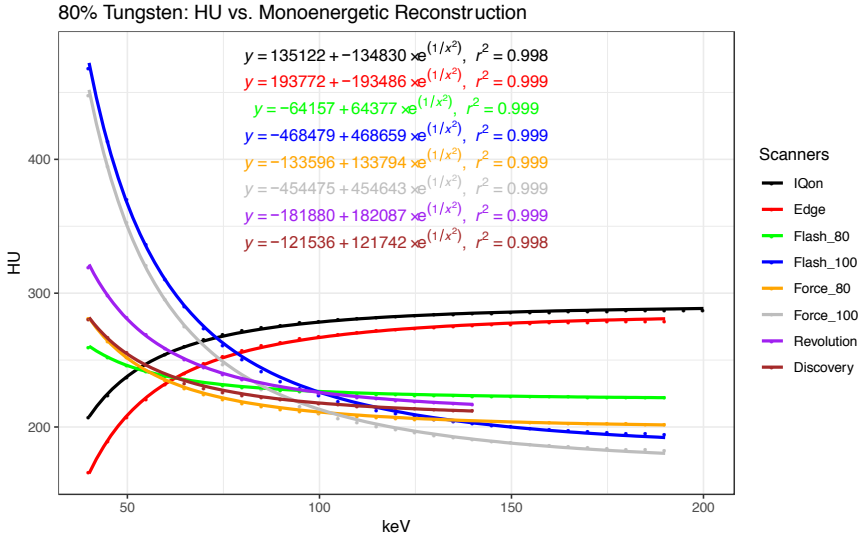

Figure 10. HU vs Monoenergetic reconstruction plots of iodine, calcium, and tungsten at concentrations 20% 40%, 60%, and 80%

Publishing Agreement

It is the policy of the University to encourage the distribution of all theses, dissertations, and manuscripts. Copies of all UCSF theses, dissertations, and manuscripts will be routed to the library via the Graduate Division. The library will make all theses, dissertations, and manuscripts accessible to the public and will preserve these to the best of their abilities, in perpetuity.

Please sign the following statement:

I hereby grant permission to the Graduate Division of the University of California, San Francisco to release copies of my thesis, dissertation, or manuscript to the Campus Library to provide access and preservation, in whole or in part, in perpetuity.

Author Signature

9 September 2019

Date